Mercury's Crustal Thickness and Contractional Strain

Thomas R. Watters[1] , **Peter B. James[2]** , **and Michelle M. Selvans[1,3]**

[1]Center for Earth and Planetary Studies, National Air and Space Museum, Smithsonian Institution, Washington, DC, USA, [2]Department of Geosciences, Baylor University, Waco, TX, USA, [3]Geology Department, Clovis Community College, Fresno, CA, USA

Abstract The crust of Mercury has experienced contraction on a global scale. Contractional deformation is expressed by a broadly distributed network of lobate thrust fault scarps. The most likely principal source of stress is global contraction from cooling of Mercury's interior. Global contraction alone would be expected to result in a uniformly distributed population of thrust faults. Mercury's fault scarps, however, often occur in long, linear clusters or bands. An analysis of the contractional strain as a function of crustal thickness, estimated in two crustal thickness models (CT1 and CT2) derived from gravity and topography data obtained during the MESSENGER mission, indicates the greatest contractional strain occurs in crust 50–60 km thick. On Earth, mantle downwelling can thicken and compress overlying crust, regionally concentrating thrust faults. Clusters of lobate scarps collocated with regions of thick crust suggest downward mantle flow contributed to the localization of lithosphere-penetrating thrust faults.

Plain Language Summary Mercury has a widespread array of fault scarps that formed by global contraction in response to the slow loss of interior heat. However, the distribution and orientations of this population of fault scarps cannot be accounted for solely by global contraction or by a combination of other sources of stress that have been proposed to date. New models of Mercury's crustal thickness show the contractional strain expressed by the fault scarps is greatest in areas of thick crust. This suggests a causal relation between the formation of thick crust and the localization of fault scarps. We propose mantle downwelling as a mechanism to thicken crust and concentrate contractional strain. Mantle downwelling is supported by a correlation between regions of modeled negative mantle dynamic pressure that induces contraction and regions of higher strain. These results support the contribution of recent and perhaps ongoing downward mantle flow in localizing major contractional faults on Mercury.

1. Introduction

An unmistakable characteristic of the surface of Mercury is the ubiquitous occurrence of contractional tectonic landforms. The first evidence of the dominance of contractional deformation was in the hemisphere imaged by Mariner 10 (Strom et al., 1975). The assumption that contractional deformation was global in extent led to the conclusion that Mercury had experienced global radial contraction (Melosh & McKinnon, 1988; Solomon, 1977; Strom et al., 1975; Watters et al.,1998, 2004). The true global distribution of contractional tectonic landforms was not revealed until the flybys and orbital phase of the MErcury Surface, Space ENvironment, GEochemistry, and Ranging (MESSENGER) mission (Solomon et al., 2008; Watters, 2021; Watters et al., 2009, 2015, Watters, Daud, et al., 2016).

Mercury's contractional tectonic landforms can be divided into three distinct and well characterized landforms; lobate scarps, high-relief ridges, and wrinkle ridges. The most broadly distributed of these are the lobate scarps (Text S1, Figure S1a). Lobate scarps have the greatest range in scale, with over 3 km of relief on the largest scarp (Watters, Montési, et al., 2016) and only tens of meters of relief on the smallest (Watters, Daud, et al., 2016). They are the expression of surface-breaking, lithosphere-penetrating, thrust faults as evidenced by the vertical offset of crosscut impact crater walls and floors (Melosh & McKinnon, 1988; Strom et al., 1975; Watters et al., 1998, 2004). Closely related to lobate scarps are the high-relief ridges (Watters et al., 2001, 2009; Figure S1b). Lobate scarps and high-relief ridges are the dominant tectonic landform in Mercury's vast intercrater plains that cover ~63% of the surface (Figures 1a and 1b). The remaining ~27% of the surface is covered by smooth plains volcanic units (Denevi et al., 2013; Head et al., 2011) that are deformed primarily by wrinkle ridges (Watters, 1988; Schleicher et al., 2019; Figure S1c). The largest expanses are found in the northern high latitudes and within and exterior to the Caloris basin (~30°N, 165°E;
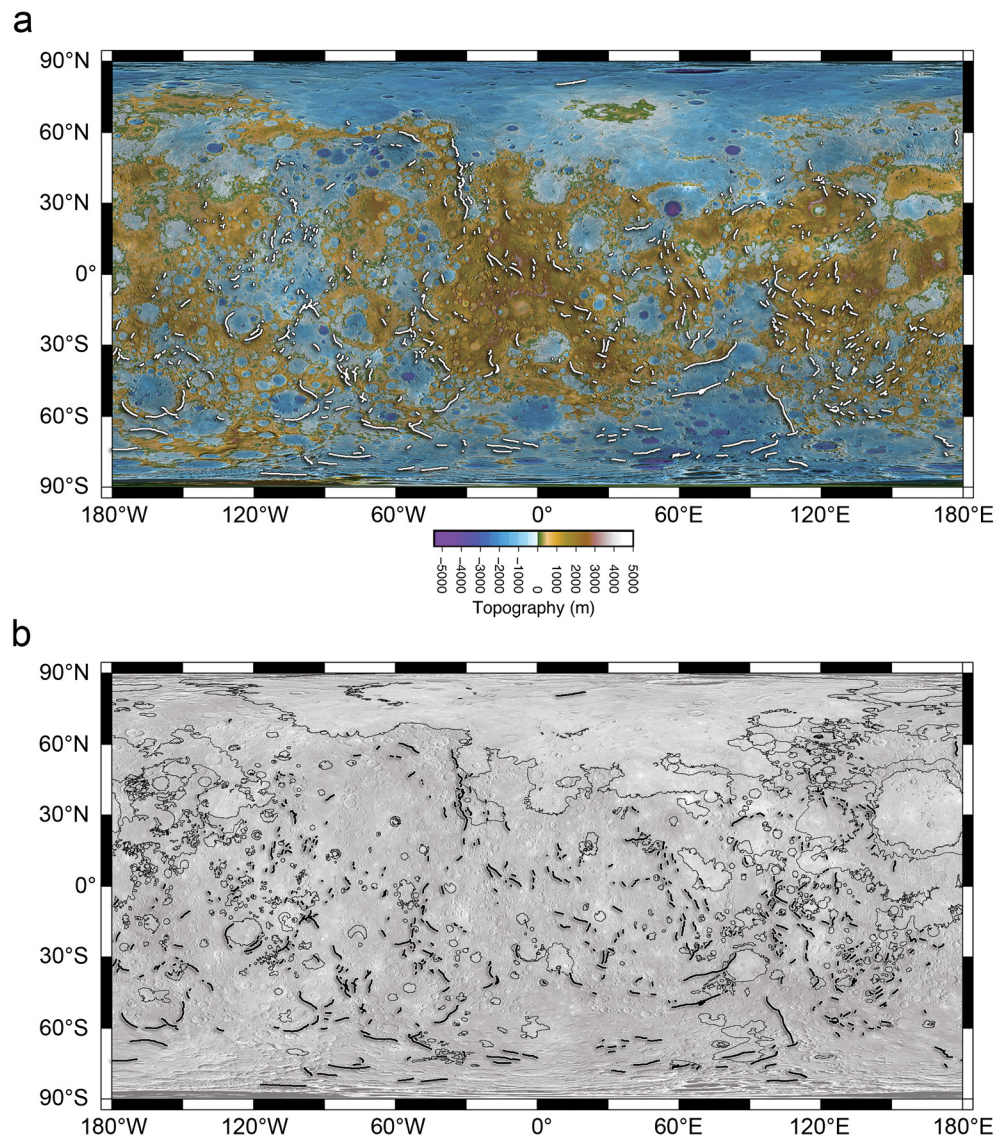
Figure 1. Mercury's lobate thrust fault scarps and high-relief ridges. (a) The locations of these contractional tectonic landforms (white polylines) are shown on the topographic map of Mercury (Becker et al., 2016). For lobate scarps the polyline is placed at the base of the vergent side of the scarp where the thrust fault breaks the surface, and for high-relief ridges the polyline is placed along the midline of the ridge indicating a blind thrust fault (Watters, 2021). (b) Lobate scarps and high-relief ridges (thick black polylines) are shown with the mapped smooth plains volcanic units (thin black lines; Denevi et al., 2013). Map projection is simple cylindrical.

Figure 1b). Wrinkle ridge thrust faults are interpreted to be shallow rooted, and deformation is thus largely confined to the smooth plains flood volcanic sequences they deform (see Watters, 1988, 2021).

The most widely accepted model for the origin of the stresses that formed Mercury's population of lobate thrust fault scarps and high-relief ridges is global radial contraction resulting from cooling of the planet's interior (Melosh & McKinnon, 1988; Solomon, 1977; Strom et al., 1975; Watters et al., 2004). Global contraction results in horizontal isotropic compressional stresses and a thrust fault population that is uniformly distributed with random orientations, given a mechanically homogenous and isotropic lithosphere. However, the lobate scarps and high-relief ridges are not uniformly distributed over the surface. They cluster in some regions and are relatively sparse to absent in others (see Figure 1; Watters, 2021; Watters et al., 2015). Here, we examine the relationship between the contractional strain expressed by the fault scarps and crustal thickness. Two models for Mercury's crustal thickness are examined along with a mantle dynamic pressure

model. The objective is to determine if regions with high contractional strain correspond to regions of greater crustal thickness and to investigate if crustal thickening has contributed to the localization of lithospheric-scale thrust faults.

2. Background

Different approaches taken in the interpretation and mapping of tectonic landforms have resulted in greatly dissimilar renderings of the population of Mercury's contractional faults (Byrne et al., 2014; Watters, 2021; Watters et al., 2009, 2015). The population of faults mapped by Watters (2021) is used in this study (Text S2). Each lobate scarp and high-relief ridge is interpreted to have a single primary thrust fault, consistent with kinematic and mechanical models of these structures (Melosh & McKinnon, 1988; Strom et al., 1975; Watters et al., 1998, 2001, 2002, 2004, 2009, 2015, Watters, Montési, et al., 2016).

The dynamic range of Mercury's topography is smaller than that found on the Moon (Zuber et al., 2012). The lower density of craters <100 km in diameter relative to the Moon suggests global volcanic resurfacing occurred just after the start of Late Heavy Bombardment (LHB; Marchi et al., 2013), contributing to the low range in elevation. The crustal thickness is well-correlated with the topography (Zuber et al., 2012). Mercury's gravity is dominated by the current subsurface structure, although most of the gravity signal can be attributed to the planet's shape (Mazarico et al., 2014; Smith et al., 2012). However, unique topographic features such as the broad rise in the northern plains (~70°N, 30°E) and long-wavelength, low amplitude undulations cutting across the interior plains of the Caloris basin (~30°N, 165°E; see Figure 1a) formed well after the emplacement and deformation of the smooth plains volcanic sequences (e.g., Zuber et al., 2012). Their associated mass anomalies may be the result of ongoing mantle flow due to either topography on the core-mantle boundary or mantle density heterogeneities (James et al., 2015). Regardless of the mechanisms that drive this mantle flow, the vertical and horizontal tractions exerted on the lithosphere by mantle flow are well constrained by Mercury's gravity field at long wavelengths.

Because lobate scarps and high-relief ridges are not uniformly distributed across the surface of Mercury (Figure 1; Text S3), other mechanisms that contribute to the nonuniform distribution of the faults must be sought. Watters et al. (2004) suggested a mechanism for generating significant horizontal compression is localized crustal thickening from mantle downwelling. The tectonics of terrestrial intraplate environments may be the best analogs to one-plate planets like Mercury. A number of intraplate locations on Earth have experience contractional deformation that appears to be caused by Rayleigh-Taylor instability of the upper mantle. Two notable examples are the thrust fault provences in central Australia and Asia (e.g., Neil & Houseman, 1999; Pysklywec & Cruden, 2004). These intraplate settings on Earth may provide insight into how large contractional landforms are localized on one-plate rocky planets in the absence of plate tectonics (Text S4).

An early model of mantle convection predicted long, linear rolls that could account for clusters of contractional landforms (King, 2008). In the post-MESSENGER view of Mercury's interior structure, the mantle is remarkably thin (~400 km), presenting a challenge to large-scale and long-lived mantle convection (Hauck et al., 2013; Michel et al., 2013; Smith et al., 2012; Tosi et al., 2013). In fact, recent models suggest that the maximum size of a convective cell is limited by the thickness of the convecting layer (Michel et al., 2013; Tosi et al., 2013). In our analysis, we consider mantle flow that is not necessarily due to convection and further consider the effects of prior variations in crustal thickness and rheology.

3. Methods

There are at least two methods by which crustal thickness (CT) maps can be constructed from gravity and topography (Zuber et al., 2012). The crust-mantle interface relief can be modeled to minimize the Bouguer gravity misfit (Wieczorek & Phillips, 1998). Alternatively, a dual inversion for the distribution of deep mass anomalies along with CT can be determined (e.g., James, 2013). The first method requires fewer parameter assumptions, but the second removes the effect of deeper mass anomalies from the CT model by incorporating dynamic flow kernels (James et al., 2015). Both methods are used to produce crustal thickness models for comparison with fault scarp locations. In both cases, we used spherical harmonic terms up to degree

and order 50, and we excluded degrees 1 and 2, which show a thickening of the crust toward the equator (Smith et al., 2012). A mean CT of 35 km is assumed, as is a mafic crustal composition with low porosity (bulk density of 2,900 kg/m^3), and a crust-mantle density contrast of 250 kg/m^3 (Nittler et al., 2011) to perform a Bouguer misfit minimization (CT1; Figure 2a, Table S1). The second CT model (CT2) is shown in Figure 2b (see Table S1). This map was derived using the same parameter values with the added assumption that topography is fully supported by a combination of crust-mantle interface relief and mantle flow. This is termed a "dual" inversion because it yields a map of mantle dynamic pressure (DP)–that is, the pressure exerted on the base of the lithosphere by mantle flow–in addition to CT. This pressure is produced by mantle flow that is driven by mantle mass anomalies just above the core-mantle boundary (350 km depth). The quality of both the gravity and the topography data are dependent on the altitude of the MESSENGER spacecraft while in Mercury orbit. Due to the elliptical orbit of the spacecraft with the pericenter in the northern high latitudes, the model results are progressively less reliable with decreasing latitude, however, the long-wavelength portion of a crustal thickness model is likely robust even in the southern hemisphere. Although there is less confidence in crustal thickness variations at <500-km length scales in the southern hemisphere, this is not expected to significantly affect the results of the analysis because most crustal thickness variations on Mercury occur at long-wavelengths (Figures 2a and 2b).

A map of DP is plotted in Figure 2c (Table S2). As with analysis of CT values, the confidence in the DP model is controlled by the availability of data in the southern hemisphere. The DP map may represent dynamic flow in the mantle in response to a perturbed intra-mantle interface or to density anomalies (James et al., 2014).

In an effort to establish the relationship between the contractional strain and crustal thickness and dynamic pressure, the CT and DP values were determined at the center latitude and longitude of each mapped contractional landform (i.e., each lobate scarp and high-relief ridge). The squares of the lengths L^2 of lobate scarps and high-relief ridges are then summed within 10 km bins of crustal thickness and 10 MPa bins of dynamic pressure. The squares of the lengths of the contractional features are then used to calculate the contractional strain. For large faults, where the fault length $L \geq$ the maximum depth of faulting, the areal contractional strain ε is given by

$$\varepsilon = \frac{\gamma \cos(\theta)}{A} \sum_{k=1}^{n} L_k^2 \tag{1}$$

where θ is the fault plane dip, A is the surface area covered by the range CT or DP values within the specified bin, n is the total number of faults, and γ is the displacement-length (D/L) ratio of the population of thrust faults associated with the lobate scarps and high-relief ridges (see Watters, 2021; Watters & Nimmo, 2010). The values of γ as a function of $\theta = 25°$, $30°$, and $35°$ are estimated from maximum relief of a representative sample of the population of lobate scarps using the best available topographic data and range from ($\sim$6.3 to 8.6) $\times 10^{-3}$ with $\gamma \cong 7.2 \times 10^{-3}$ for $\theta = 30°$ (Watters, 2021). The contractional strain is thus estimated from the sum of the squares of the lengths of the faults in the specified bin of CT or DP.

4. Results

The range in crustal thickness in the CT1 model is $\sim$11–73 km with a mean of $\sim$35 km, and $\sim$7–74 km in the CT2 model with a mean of also $\sim$35 km (Table S3). The median crustal thickness from CT1 and CT2 models is $\sim$33 and $\sim$34 km, respectively. The greatest areal contractional strain ε as a function of crustal thickness is found in the 55 km bin (range 50–60 km) for both the CT1 and CT2 models (Figures 3a and 3b). The contractional strain in the 55 km bin of the CT1 model ranges from $\sim$0.14 to 0.21% with $\varepsilon \cong 0.17\%$ at $\theta = 30°$ (Figure 3a). The contractional strain in the 55 km bin of the CT2 model is very similar to the CT1, ranging from $\sim$0.13 to 0.20% with $\varepsilon \cong 0.16\%$ at $\theta = 30°$ (Figure 3b). This analysis clearly indicates that greatest contractional strain is found in areas of greater crustal thickness (Figures 2a and 2b).

In order to test if the observed spatial correlation is not simply a random effect, 10 random populations of 651 thrust faults, the number of faults in the Watters (2021) data set, with random globally distributed fault center locations and with random lengths were generated. A weighted gamma function was used to create random populations of lengths with a frequency distribution and total cumulative length approximating the
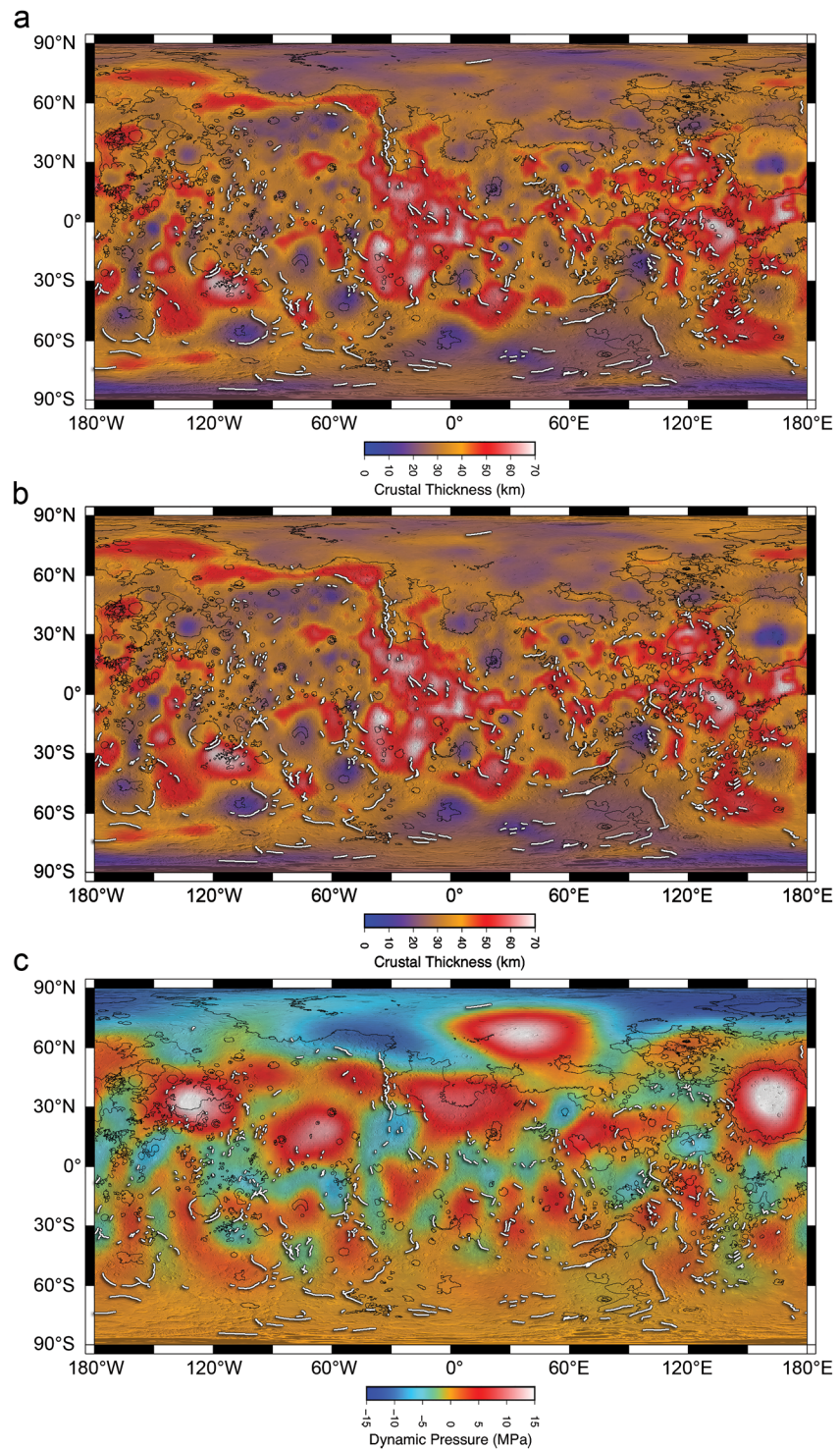
Figure 2. Models of Mercury's crustal thickness and mantle dynamic pressure. (a) Elastic crustal thickness model (CT1). (b) Dual inversion crustal thickness model (CT2). The resolution of the CT models are 1° per pixel. (c) The mantle dynamic pressure model (DP). The resolution of the DP model is 1° per pixel. The locations of mapped contractional landforms are shown for comparison (white lines). The locations of smooth plains volcanic units (Denevi et al., 2013) are outlined (thin black lines). The confidence in CT and DP values for the models is limited by the quality of the gravity and topography data in the southern hemisphere.
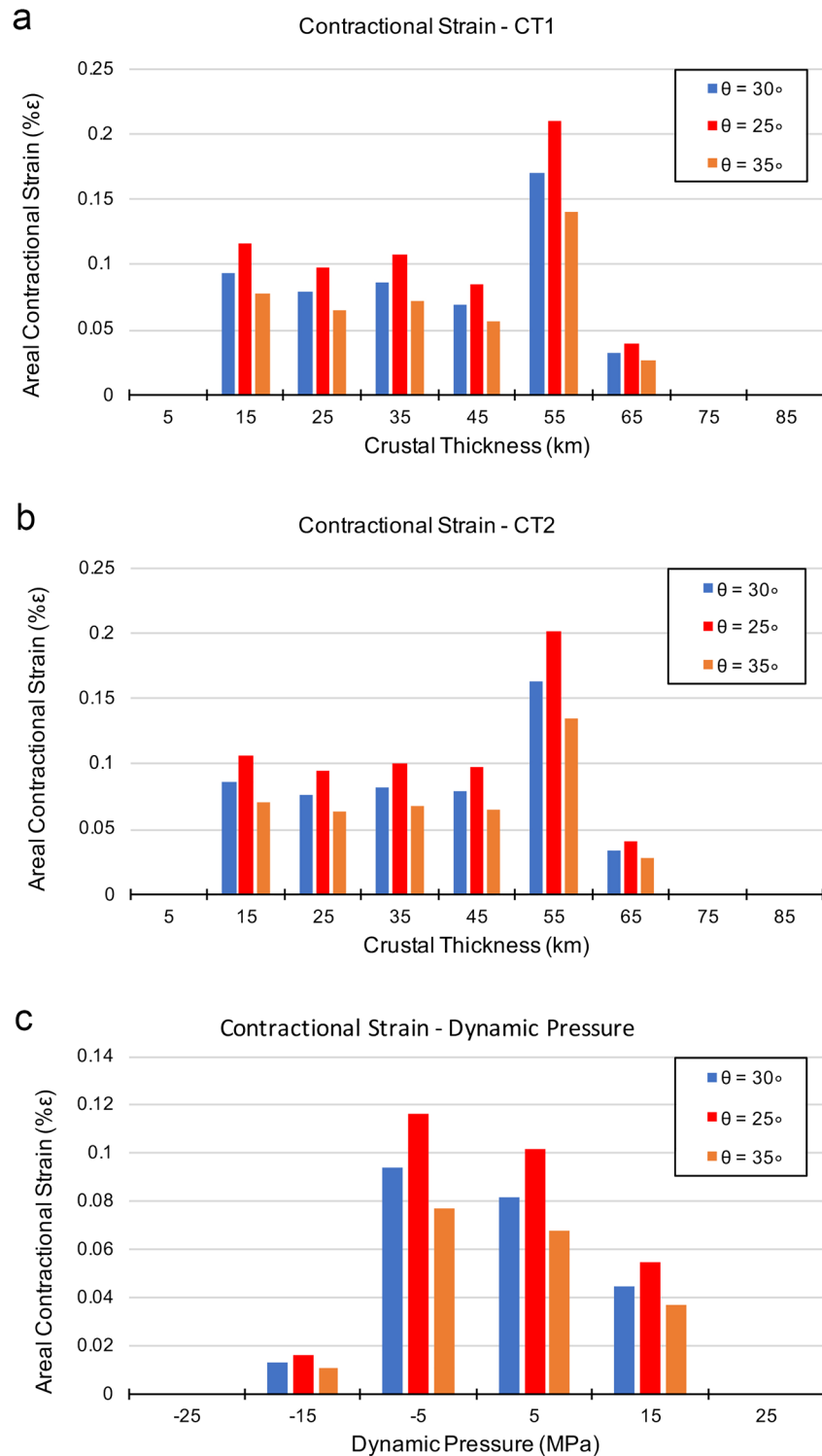
Figure 3. Contractional strain as a function of crustal thickness and mantle dynamic pressure. (a) Areal contractional strain estimated in 10 km bins for the crustal thickness (CT1) crustal thickness model. (b) Areal contractional strain estimated in 10 km bins for the CT2 crustal thickness model. (c) Areal contractional strain estimated in 10 MPa bins for the dynamic pressure model. The contractional strain is estimated using three values of the fault-plane dip θ. Crustal thickness bins with <1.0% of the total surface area of the planet are not considered statistically signficant and are not included (see Supporting Table S1 and S2).

651 mapped fault population. The analysis shows that none of the random fault population models produce a peak strain >0.09% (for $\theta = 30°$) in the higher-than-average model crustal thickness bins of 45 and 55 km for either the CT1 or CT2 models (Figures S2 and S3). Only one random population (Random Model 6–CT1) produces a peak strain that exceeds 0.09% (for $\theta = 30°$) in the 65 km bin. Thus, it is concluded that the null hypothesis – the observed correlation between clusters of faults and thick crust is a random effect – can be rejected.

There are notable spatial correlations between clusters of thrust fault scarps and regions of thick crust. One of the most striking is the Victoria Rupes cluster of lobate scarps and high-relief ridges (∼35ºN, 30ºW; Figures 2a and 2b). This cluster, that includes Victoria Rupes (∼51.7°N, −34.0°W), Endeavor Rupes (∼38.4°N, 31.5°W), and Antoniadi Dorsa (∼30°N, 31.2°W), extends over 1,500 km. These large structures contribute to the cumulative length of one of the major longitudinal deformation bands on Mercury (Watters, 2021; Watters et al., 2015). It is also notable that the cluster of faults occurs on the eastern border of a long, linear region of thick crust oriented roughly north-south. At its northernmost extent, this region of thick crust is oriented roughly east-west and forms the local boundary with the northern smooth plains (Figures 2a and 2b). Here, another prominent lobate scarp, Carnegie Rupes (∼58.3°N, 53.5°W), occurs along the southern border of the region of thick crust.

The range in model dynamic pressure is from approximately −15 to 19 MPa with a mean of 0 MPa (Table S3). The greatest contractional strain is found in the −5 MPa bin (range −10–0 MPa) of DP (Figure 2c) with $\varepsilon \cong 0.09\%$ at $\theta = 30°$. The contractional strain in the −5 MPa bin is ∼15% (0.012% at $\theta = 30°$) greater than in the 5 MPa bin, and more than a factor of 2 greater than in the 15 MPa bin ($\theta = 30°$; Figure 3c). Thus, there is a significant correlation between peak contractional strain and negative dynamic pressure. There are also areas with clear spatial correlation between regions of low and high dynamic pressure and clusters of fault scarps, with some clusters located near transitions of negative and positive dynamic pressure (Figures 2c and 3).

5. Discussion

The analysis shows that the locations of fault scarps on Mercury are not randomly distributed with respect to modeled CT values, either for the elastic model (CT1) or for the model that includes mantle dynamics (CT2). In both cases, the contractional strain is greatest where the crust is thick (Figures 3a and 3b). This spatial correlation between areas of thick crust and greatest contractional strain suggests that mantle downwelling may have significantly influenced the localization and development of many of the major thrust faults, adding a localized component of lithospheric stress to the isotropic stress due to global contraction.

Variations in crustal density due to compositional variations or impact-driven porosity may lead to some uncertainty in any crustal thickness model. For example, Beuthe et al. (2020) used surface mineralogy derived from MESSENGER data to infer lateral variations in crustal density and the degree of mantle melting. Additionally, they assumed the existence of near-surface porosity profiles comparable to those observed on the Moon. A comparable analysis of two crustal thickness models of Beuthe et al. (2020), V0 and V8 (Figure S4, Table S4), shows relatively small peaks in contractional strain in thick crust (Figure S5). In both models, the peak strain occurs in the 45 km bin (V0, $\varepsilon \cong 0.11\%$, and V8, $\varepsilon \cong 0.13\%$ at $\theta = 30°$). Beuthe et al. (2020) find the thickest crust in the V0 model corresponds to the high-Mg terrain (∼30°N, 110°W) identified in MESSENGER X-ray spectrometer data (Weider et al., 2015; Figure S6). The CT1 and CT2 models presented here do not show generally thick crust in the high-Mg terrain (Figure S7). The exceptions are a few isolated regions, the most significant of which is near ∼30°N, 80°W that corresponds to the area of peak crustal thickness in the Beuthe et al. (2020) V0 model (Figure S6). Moreover, a comparison of the contractional landforms with the two mantle melt crustal thickness model (V0 and V8) shows no obvious relation between the number or orientation of mapped faults and the high-Mg terrain (Figure S4). The analysis shows that mapped faults are correlated with moderately thick crust for the models of Beuthe et al., similar to the correlation that we report for CT1 and CT2 (Figure S5). Therefore, this correlation appears to be robust for a wide range of plausible assumptions about Mercury's internal structure.

Contractional strain is significantly greater in regions of negative (compressional) dynamic pressure (Figure 3c). These results are consistent with downward flow in the mantle contributing to a stress environment

that favors the development of thrust faults in Mercury's lithosphere. While the contribution of stresses imparted by the mantle may be small relative to other sources of stress in the lithosphere (e.g., global contraction), the statistically significant correlation suggests that mantle flow nevertheless contributes to the geographic distribution of tectonic structures. While we can only infer present-day dynamic pressure from Mercury's gravity field, a correlation between negative dynamic pressure and contractional strain suggests that the observed flow patterns may be similar to the flow patterns that existed during the formation of some lobate scarps.

The contractional strain is lower in both CT1 and CT2 models in areas with thin crust, relative to areas of thick crust (>50 km) with the exception of the thickest crust (>60 km; Figures 3a and 3b) which makes up ≤2% the surface area (Table S1). This is consistent with mantle flow thickening the crust and enhancing contractional strain at locations of mantle downwelling and inward lower crustal flow. A number of mechanisms may account for mantle flow on Mercury, including compositional buoyancy heterogeneities in an otherwise stagnant mantle, thermochemical mantle convection, and/or localized gravitational instability of the mantle. The trigger for gravitational instability of Mercury's mantle, as has been proposed for the Earth, may be presence of remote stresses (Neil & Houseman, 1999). A likely source of remote compressional stresses on Mercury is global contraction. The downward flow process of thickening crust is expected to also thin the crust in some areas. At locations with a net loss of lower crustal material as a result of lateral flow, there may be some extensional stress imparted to the overlying brittle layer (Pysklywec & Cruden, 2004). Extensional tectonic features are only observed within impact basins and some buried (ghost) craters and basins on Mercury (e.g., Watters et al., 2009, 2012). Therefore, it is expected that the potential contribution to the stress field from extensional stresses in areas of crustal thinning do not exceed compressional stresses due to global contraction and may contribute to lower contractional strain in areas of thinnest crust. Moreover, the regions of thinnest crust generally correspond to longitudal bands with the smallest cumulative length of fault scarps (see Watters, 2021; Watters et al., 2015).

The two models of crustal thickness rely on different assumptions about the mechanisms of topographic compensation: the CT1 model allows topography to be partially uncompensated (i.e., partially supported by elastic stresses), whereas the dual inversion associated with the CT2 model is based on the assumption that the combination of crustal thickness variations and deep-seated dynamic pressure entirely support topography. These two models therefore represent two endmember scenarios for the support of Mercury's topography. Our results indicate that, regardless of whether long-wavelength topography is in part supported by dynamic or by elastic stresses (or both), the mechanical lithosphere has preferentially developed thrust faults in areas with the thickest crust.

Model results for the dual inversion are consistent with a long-lasting, stationary pattern of mantle flow (perhaps convective motion) that thickened the crust and localized thrust fault scarps. Preexisting variations in crustal thickness and/or rheology (e.g., Montési & Zuber, 2002) may have also influenced the observed fault pattern, as noted for several prominent fault scarps localized by basin rims (e.g., Fassett et al., 2012; Watters et al., 2015). Crosscutting relations with impact craters of differing ages and degradation states suggest thrust faults have been actively developing on Mercury since the Calorian (∼3.9 Ga; Banks et al., 2015), and the discovery of small-scale lobate scarps indicates thrust faulting may be ongoing (Watters, Daud, et al., 2016). This supports a long-lived period of contractional deformation, perhaps contributed to by a period of relatively stationary mantle flow.

While lobate scarps and high-relief relief are generally associated with areas of thick crust, smooth plains volcanic units, dominated by wrinkle ridges, are associated with areas of thinner crust in the northern hemisphere. The northern smooth plains are underlain by relatively thin crust, generally <40 km thick in both CT1 and CT2 (Figures 2a and 2b). This is also mostly the case for the smooth plains of Suisei Planitia (∼60°N, 150°W), Buda Planitia (∼20°N, 150°W), and Sobkou Planitia (∼40°N, 130°W), and much of the Caloris basin (∼30°N, 165°E). Exceptions are some margins of the Caloris basin and much of the Caloris exterior smooth plains. Thin crust associated with smooth plains is also indicated in the mantle melt crustal thickness model of Beuthe et al. (2020) (Figure S6). Their model shows thin crust in the geochemically distinct terrains of the northern smooth plains and Caloris where lithospheric-scale thrust faults are largely absent (see Figures S4 and S6).

The smooth ridged-plains were likely deformed by stresses from subsidence and flexure of thinner or weaker lithosphere due to loads of basalt-like volcanics that locally dominated stresses from global contraction (see Schleicher et al., 2019; Watters, 2021). Variations in effective elastic thickness T_e on Earth generally correlate with variations in crustal thickness T_c. Thus, low values of T_c generally correspond to low values of T_e (Djamani et al., 1995) and the thickness of the seismogenic crust (Maggi et al., 2000). If this is also the case for Mercury, the smooth plains in the northern hemisphere might be expected to be supported by relatively thin elastic lithosphere. The sparsity of lithosphere-penetrating thrust faults in the expanses of northern smooth plains could be explained by the effects of large basin-forming impacts that would have locally reset the compressive stresses from global contraction. It has been suggested that the dichotomy in contractional strain between the northern and southern hemispheres is due to a generally thicker, stronger elastic lithosphere in the northern hemisphere that inhibited formation of lithosphere-penetrating thrust faults (Watters, 2021). Alternatively, based on the results of this study, the greater contractional strain found in the southern hemisphere may be due to a greater contribution of mantle flow in thickening the crust and localizing deeply rooted thrust faults. Additional gravity data collected by the BepiColombo spacecrafts will support improved crustal thickness models for Mercury and further analysis of the relation with contractional strain.

In summary, lithospheric contractional strain is greatest in areas of thick crust, suggesting a causal relation between the formation of thick crust and the localization of fault scarps. Regions of thinner crust are largely devoid of lithosphere-penetrating contractional landforms. Mantle downwelling may enhance strain from global contraction in regions of thickened crust, and is supported by the correlation between regions with negative mantle dynamic pressure and higher contractional strain. These results suggest recent and perhaps ongoing mantle flow has a role in localizing lithosphere-penetrating thrust faults on Mercury.

Data Availability Statement

Data are available on the Smithsonian's Figshare site (https://smithsonian.figshare.com/articles/dataset/Mercury_s_crustal_thickness_and_contractional_strain/14270720). The raw and calibrated image data that support the findings of this study are available from Planetary Data System Cartography and Imaging Sciences Node (https://pds-geosciences.wustl.edu/missions/messenger/index.htm).

References

Banks, M. E., Xiao, Z., Watters, T. R., Strom, R. G., Braden, S. E., Chapman, C. R., et al. (2015). Duration of activity on lobate-scarp thrust faults on Mercury. *Journal of Geophysical Research: Planets*, *120*, 1751–1762. https://doi.org/10.1002/2015JE004828

Becker, K. J., Robinsin, M. S., Becker, T. L., Weller, L. A., Edmundson, K. L., Neumann, G. A., et al. (2016). First global digital elevation model of Mercury (Abstract). *Lunar and Planetary Science*, *47*, 2959.

Beuthe, M., Charlier, B., Namur, O., Rivoldini, A., & Van Hoolst, T. (2020). Mercury's crustal thickness correlates with lateral variations in mantle melt production. *Geophysical Research Letters*, *47*. https://doi.org/10.1029/2020GL087261

Byrne, P. K., Klimczak, C., Şengör, A. M. C., Solomon, S. C., Watters, T. R., & Hauck, S. A., II. (2014). Mercury's global contraction much greater than previous estimates. *Nature Geoscience*, *7*, 301–307. https://doi.org/10.1038/ngeo2097

Denevi, B. W., Ernst, C. M., Meyer, H. M., Robinson, M. S., Murchie, S. L., Whitten, J. L., et al. (2013). The distribution and origin of smooth plains on Mercury. *Journal of Geophysical Research: Planets*, *118*, 891–907. https://doi.org/10.1002/jgre.20075

Djamani, Y. H. P., Nnange, J. M., Diament, M., Ebinger, C. J., & Fairhead, J. D. (1995). Effective elastic thickness and crustal thickness variations in west central Africa inferred from gravity data. *Journal of Geophysical Research*, *100*(B11), 22047–22070.

Fassett, C. I., Head, J. W., Baker, D. M. H., Zuber, M. T., Smith, D. E., Neumann, G. A., et al. (2012). Large impact basins on Mercury: Global distribution, characteristics, and modification history from MESSENGER orbital data. *Journal of Geophysical Research*, *117*(E12), E00L08. https://doi.org/10.1029/2012JE004154

Hauck, S. A., Margot, J.-L., Solomon, S. C., Phillips, R. J., Johnson, C. L., Lemoine, F. G., et al. (2013). The curious case of Mercury's internal structure. *Journal of Geophysical Research: Planets*, *118*, 1204–1220. https://doi.org/10.1002/jgre.20091

Head, J. W., Chapman, C. R., Strom, R. G., Fassett, C. I., Denevi, B. W., Blewett, D. T., et al. (2011). Flood volcanism in the northern high latitudes of Mercury revealed by MESSENGER. *Science*, *333*, 1853–1856. https://doi.org/10.2226/science.1211997

James, P. B. (2013). *Geophysical insights into the histories of Venus, Mercury, and the Moon* (Ph. D. Thesis). Massachusetts Institute of Technology.

James, P. B., Solomon, S. C., Zuber, M. T., & Phillips, R. J. (2014). What Mercury's topographic rises tell us about the interior (Abstract). *Lunar and Planetary Science*, *45*, 1452.

James, P. B., Zuber, M. T., Phillips, R. J., & Solomon, S. C. (2015). Support of long-wavelength topography on Mercury inferred from MESSENGER measurements of gravity and topography. *Journal of Geophysical Research: Planets*, *120*(2), 287–310. https://doi.org/10.1002/2014JE004713

King, S. D. (2008). Pattern of lobate scarps on Mercury's surface reproduced by a model of mantle convection. *Nature Geoscience*, *1*, 229–232. https://doi.org/10.1038/ngeo152

Maggi, A., Jackson, J. A., McKenzie, D., & Priestley, K. (2000). Earthquake focal depths, effective elastic thickness, and the strength of the continental lithosphere. *Geology*, *28*, 495–498. https://doi.org/10.1130/0091-7613(2000)028<0495:efdeet>2.3.co;2

Marchi, S., Chapman, C. R., Fassett, C. I., Head, J. W., Bottke, W. F., & Strom, R. G. (2013). Global resurfacing of Mercury 4.0–4.1 billion years ago by heavy bombardment and volcanism. *Nature*, *499*, 59–61. https://doi.org/10.1038/nature12280

Mazarico, E., Genova, A., Goossens, S., Lemoine, F. G., Neumann, G. A., Zuber, M. T., et al. (2014). The gravity field, orientation, and ephemeris of Mercury from MESSENGER observations after three years in orbit. *Journal of Geophysical Research: Planets*, *119*, 2417–2436. https://doi.org/10.1002/2014JE004675

Melosh, H. J., & McKinnon, W. B. (1988). The tectonics of Mercury. In F. Vilas, C. R. Chapman, & M. S. Matthews (Eds.), *Mercury* (p. 374–400). Tucson: University of Arizona Press.

Michel, N. C., Hauck, S. A., II, Solomon, S. C., Phillips, R. J., Roberts, J. H., & Zuber, M. T. (2013). Thermal evolution of Mercury as constrained by MESSENGER observations. *Journal of Geophysical Research: Planets*, *118*, 1033–1044. https://doi.org/10.1002/jgre.20049

Montési, L. G. J., & Zuber, M. T. (2002). A unified description of localization for application to large-scale tectonics. *Journal of Geophysical Research*, *107*(B3). https://doi.org/10.1029/2001JB000465

Neil, E. A., & Houseman, G. A. (1999). Rayleigh-Taylor instability of the upper mantle and its role in intraplate orogeny. *Geophysical Journal International*, *138*, 89–107. https://doi.org/10.1046/j.1365-246x.1999.00841.x

Nittler, L. R., Starr, R. D., Weider, S. Z., McCoy, T. J., Boynton, W. V., Ebel, D. S., et al. (2011). The major-element composition of Mercury's surface from MESSENGER x-ray spectrometry. *Science*, *333*, 1847–1850. https://doi.org/10.1126/science.1211567

Pysklywec, R. N., & Cruden, A. R. (2004). Coupled crust-mantle dynamics and intraplate tectonics: Two-dimensional numerical and three-dimensional analogue modeling. *Geochemistry, Geophysics, Geosystems*, *5*, Q10003. https://doi.org/10.1029/2004GC000748

Schleicher, L. S., Watters, T. R., Martin, A. J., & Banks, M. E. (2019). Wrinkle ridges on Mercury and the Moon within and outside of Mascons. *Icarus*, *331*, 226–237. https://doi.org/10.1016/j.icarus.2019.04.013

Smith, D. E., Zuber, M. T., Phillips, R. J., Solomon, S. C., Hauck, S. A., Lemoine, F. G., et al. (2012). Gravity field and internal structure of Mercury from MESSENGER. *Science*, *336*, 214–217. https://doi.org/10.1126/science.1218809

Solomon, S. C. (1977). The relationship between crustal tectonics and internal evolution in the Moon and Mercury. *Physics of the Earth and Planetary Interiors*, *15*, 135–145. https://doi.org/10.1016/0031-9201(77)90026-7

Solomon, S. C., McNutt, R. L., Watters, T. R., Lawrence, D. J., Feldman, W. C., Head, J. W., et al. (2008). Return to Mercury: A global perspective on MESSENGER's first Mercury flyby. *Science*, *321*, 59–62. https://doi.org/10.1126/science.1159706

Strom, R. G., Trask, N. J., & Guest, J. E. (1975). Tectonism and volcanism on Mercury. *Journal of Geophysical Research*, *80*, 2478–2507. https://doi.org/10.1029/JB080i017p02478

Tosi, N., Grott, M., Plesa, A.-C., & Breuer, D. (2013). Thermochemical evolution of Mercury's interior. *Journal of Geophysical Research: Planets*, *118*, 2474–2487. https://doi.org/10.1002/jgre.20168

Watters, T. R. (1988). Wrinkle ridge assemblages on the terrestrial planets. *Journal of Geophysical Research*, *93*, 10236–10254. https://doi.org/10.1029/jb093ib09p10236

Watters, T. R. (2021). A case for limited global contraction of Mercury. *Communications Earth & Environment*, *2*, 2. https://doi.org/10.1038/s43247-020-00076-5

Watters, T. R., Daud, K., Banks, M. E., Selvans, M. M., Chapman, C. R., & Ernst, C. M. (2016). Recent tectonic activity on Mercury revealed by small thrust fault scarps. *Nature Geoscience*, *9*, 743–747. https://doi.org/10.1038/ngeo2814

Watters, T. R., Montési, L. G. J., Oberst, J., & Preusker, F. (2016). Fault-bound valley associated with the Rembrandt Basin on Mercury. *Geophysical Research Letters*, *43*, 11536–11544. https://doi.org/10.1002/2016GL070205

Watters, T. R., & Nimmo, F. (2010). The tectonics of Mercury. In T. R. Watters, & R. A. Schultz (Eds.), *Planetary tectonics*. (pp. 15–80). Cambridge: Cambridge University Press.

Watters, T. R., Robinson, M. S., Bina, C. R., & Spudis, P. D. (2004). Thrust faults and the global contraction of Mercury. *Geophysical Research Letters*, *31*, L04701. https://doi.org/10.1029/2003GL019171

Watters, T. R., Robinson, M. S., & Cook, A. C. (1998). Topography of lobate scarps on Mercury: New constraints on the planet's contraction. *Geology*, *26*, 991–994. https://doi.org/10.1130/0091-7613(1998)026<0991:tolsom>2.3.co;2

Watters, T. R., Robinson, M. S., & Cook, A. C. (2001). Large-scale lobate scarps in the southern hemisphere of Mercury. *Planetary and Space Science*, *49*, 1523–1530. https://doi.org/10.1016/s0032-0633(01)00090-3

Watters, T. R., Schultz, R. A., & Robinson, M. S., & Cook, A. C. (2002). The mechanical and thermal structure of Mercury's early lithosphere. *Geophysical Research Letters*, *29*. https://doi.org/10.1029/2001GL014308

Watters, T. R., Selvans, M. M., Banks, M. E., Hauck, S. A., II, Becker, K. J., & Robinson, M. S. (2015). Distribution of large-scale contractional tectonic landforms on Mercury: Implications for the origin of global stresses. *Geophysical Research Letters*, *42*, 3755–3763. https://doi.org/10.1002/2015GL063570

Watters, T. R., Solomon, S. C., Klimczak, C., Freed, A. M., Head, J. W., Ernst, C. M., et al. (2012). Extension and contraction within volcanically buried impact craters and basins on Mercury. *Geology*, *40*, 1123–1126. https://doi.org/10.1130/g33725.1

Watters, T. R., Solomon, S. C., Robinson, M. S., Head, J. W., André, S. A., Hauck, S. A., II, & Murchie, S. L. (2009). The tectonics of Mercury: The view after MESSENGER's first flyby. *Earth and Planetary Science Letters*, *285*, 283–296. https://doi.org/10.1016/j.epsl.2009.01.025

Weider, S. Z., Nittler, L. R., Starr, R. D., Crapster-Pregont, E. J., Peplowski, P. N., Denevi, B. W., et al. (2015). Evidence for geochemical terranes on Mercury: Global mapping of major elements with MESSENGER's X-ray spectrometer. *Earth and Planetary Science Letters*, *416*, 109–120. https://doi.org/10.1016/j.epsl.2015.01.023

Wieczorek, M. A., & Phillips, R. J. (1998). Potential anomalies on a sphere: Applications to the thickness of the lunar crust. *Journal of Geophysical Research*, *103*, 1715–1724. https://doi.org/10.1029/97JE03136

Zuber, M. T., Smith, D. E., Phillips, R. J., Solomon, S. C., Neumann, G. A., Hauck, S. A., et al. (2012). Topography of the northern hemisphere of Mercury from MESSENGER laser altimetry. *Science*, *336*, 217–220. https://doi.org/10.1126/science.1218805

Reference From the Supporting Information

Di Achille, G., Popa, C., Massironi, M., Mazzotta Epifani, E., Zusi, M., Cremonese, G., & Palumbo, P. (2012). Mercury's radius change estimates revisited using MESSENGER data. *Icarus*, *221*, 456–460. https://doi.org/10.1016/j.icarus.2012.07.005